Electrical Power and Energy Systems 87 (2017) 211–221

Contents lists available at ScienceDirect

Electrical Power and Energy Systems

journal homepage: www.elsevier.com/locate/ijepes

Simple bottom-up hierarchical control strategy for heaving wave energy converters

A. Wahyudie [a,*], M.A. Jama [a], T.B. Susilo [b], O. Saeed [a], C.S.A. Nandar [c], K. Harib [d]

[a] Electrical Engineering Department, United Arab Emirates University (UAE-U), United Arab Emirates
[b] Electrical Engineering Department, King Fath University of Petroleum and Minerals, Saudi Arabia
[c] Agency for Assessment and Application of Technology, Indonesia
[d] Mechanical Engineering Department, UAE-U, United Arab Emirates

ARTICLE INFO

Article history:
Received 3 November 2015
Received in revised form 12 September 2016
Accepted 26 October 2016
Available online 7 November 2016

Keywords:
Heaving wave energy converters
Hierarchical control strategy
Lead-lag compensator
Marine energy
Robust control

ABSTRACT

The objective of this study was to improve the power captured in heaving wave energy converters using a simple robust hierarchical control strategy (HCS). A HCS comprises a higher level controller (HLC) and a lower level controller (LLC). The HLC provides a reference velocity for the buoy, which is in-phase with the wave's excitation force. The LLC follows the reference despite the uncertainties in the model. We propose a new HCS called bottom-up HCS (BU-HCS), where the LLC is designed before the HLC. The LLC is implemented using a feedback controlled system with a simple lead-lag compensator as its controller. The lead-lag compensator is designed using $\mathcal{H}_\infty$ theory with the objectives of maximizing the robustness and tracking properties of the LLC while minimizing the control force of the power take-off (PTO) device. A set of optimization problem is obtained for designing the parameters of the lead-lag compensator, which are solved using a genetic algorithm. The HLC in the BU-HCS provides the velocity reference, which satisfies a constraint on the control force and the PTO's utilization index. The HLC is implemented by designing the value of an intrinsic resistance constant, which can be found using the Bode magnitude plot of a transfer function. Based on the plot, a look-up table for the intrinsic resistance constant is generated as a function of the significant height and the peak period of the wave. We tested the proposed method in various scenarios and its performance was compared with existing control techniques.

1. Introduction

One of the most promising renewable energy resources is marine energy and it has been estimated that the global marine energy potential is around 32 TW. The current marine energy market comprises tidal energy, wave energy, and energy generated from ocean salinity and temperature differences [1]. Wave energy has an estimated global potential of 2 TW, which is almost equivalent to the world's electricity consumption. However, due to the irregularity of wave resources as well as the physical constraints to construct a power take-off (PTO) in wave energy converters (WECs), only 25% of the available potential can be harnessed (i.e., 0.5 TW) [2].

Various control strategies have been proposed to enhance the power-to-cost ratio of WECs. An appropriately designed control strategy can improve the WEC capture width, impose system limitations, make the system less susceptible to model imperfections and external disturbances, and provide adequate support to the power take-off (PTO) mechanism [3]. The simplest forms of control for heaving WECs are passive control strategies (e.g., resistive and reactive loading), which lack reference signal tracking (i.e., open loop control) [4]. Although they are simple and cost-effective, these passive control strategies are usually designed based on a single frequency per sea state. Therefore, the performance of the controlled system is lower at other frequencies. In addition, methods based on heuristic control strategies have been reported previously, e.g., fuzzy-based controllers [5,6]. Many predictive control strategies have also been proposed (e.g., see [7,8]). Predictive controllers can produce the optimum control effort and introduce system constraints into the control problem, but greater computational capacities are required since a constrained optimization problem is solved at each sampling instance. Furthermore, predictive controllers are model-based techniques and thus extra measures are required to prevent modelling mismatches. The other category of controllers comprises reference-based control techniques, where a desired signal is tracked in a feedback controlled system. The reference signal is often selected as the heave velocity of the WEC's floater, which is determined

* Corresponding author.
E-mail address: addy.w@uaeu.ac.ae (A. Wahyudie).

http://dx.doi.org/10.1016/j.ijepes.2016.10.010
0142-0615/

based on the principle of maximum power transfer [9]. This is usually formulated as a hierarchical control strategy (HCS), which comprises a higher level controller (HLC) responsible for generating the reference signal and a lower level controller (LLC) that performs reference tracking. In [10], a simple HCS was proposed, where the LLC utilizes a lead compensator, whereas an ultra-local model principle is used to compensate for the model uncertainties and un-modelled dynamics. In [11,12], internal mode control was employed in the LLC as a measure to improve the controllers robustness. In [13], the reference-based method was combined with predictive control, where the velocity reference to be followed was generated using model predictive control (MPC).

In this study, we propose a new form of hierarchical control for WECs called bottom-up HCS (BU-HCS), which improves the existing HCS methods. The generation of the reference velocity for the HLC proposed by [11,13,12] is based on the radiation resistance value of the floater/buoy. However, this approach has a major drawback because the HCS is tuned only over a single wave's frequency. This is impractical because irregular sea states contain a mix of incoming frequencies that can be represented in a spectrum. Recently, this drawback was addressed by [10,14], who used the intrinsic resistance to construct the velocity reference, which could be varied based on the significant height and peak frequency of the wave within an interval of time. However, the algorithm required to design the intrinsic resistance is complex. The proposed BU-HCS provides a much simpler method for finding the intrinsic resistance as a function of the wave's significant height and peak frequency. Moreover, the HLC in the BU-HCS incorporates a constraint on the maximum value of the control force from the PTO device and thus PTO utilization. The PTO utilization is defined as the ratio of the maximum converted power relative to the average converted power. In order to limit the control force in BU-HCS, the intrinsic resistance is not designed using the topology of the buoy alone. The design process also involves a dynamic model of the LLC. Thus, in the BU-HCS, there is an interconnection process during the designing of the LLC and the HLC, where the LLC is designed before the HLC in the BU-HCS. Robust tracking controllers (i.e., internal mode control, sliding mode control, and model-free control) are used in the LLC, as proposed by [10–12]. However, there is no physical constraint consideration during the LLC design process. The constraints on the control force, buoy position, and velocity were considered using a MPC by [13], but the MPC incurs high computational costs and it is prone to model uncertainty. In the proposed BU-HCS, a simple lead-lag compensator is used as the main controller in the LLC to provide a good tracking controller and robustness against the model uncertainties and disturbance, as well as minimizing the control force in the system. Therefore, many new features are provided by the BU-HCS compared with the existing HCS.

The remainder of this paper is organized as follows. The mathematical model of the WEC is described in Section 2. The proposed control strategy is given in Section 3. The simulation setup and results are given in Section 4. Finally, we give our conclusions in Section 5.

2. Mathematical modelling

In this study, we consider the Upsalla single-body sea-based heaving WECs, as depicted in Fig. 1. The WEC comprises a buoy, a tether, and a PTO. The PTO comprises a permanent magnet linear generator (PMLG) and a power converter module. The power converter is set up in a back-to-back scheme, where the machine-side converter (MSC) is responsible for controlling the heave velocity of the PMLG by regulating the machine stator current. The grid-side converter is employed to smooth the power before sending it to the grid. The DC-link maintains the instantaneous power balance between the two sides of the converter. The PTO has two roles, i.e., generating electricity and providing the control force to maximize energy absorption from the wave. The PTO can maximize the energy absorption by applying a damping force on the buoy so the buoy's velocity moves in phase with the excitation force. The damping force can be generated by controlling the current in the stator of the PMLG. The current can be regulated using the switches in the power converter module.

The mathematical model of the WEC comprises mechanical and electrical models. The details of these models are described in the following sections.

2.1. Mechanical model

The mechanical model describes the forces acting on the WEC buoy. In this study, a linear approximation is used in the mechanical model, where the buoy's elevation $z(t)$ is around an equilibrium point. In the linear approximation, the dynamics of the buoy are described using the following equation

$$f_e(t) - f_r(t) - f_b(t) - f_l(t) - f_s(t) + f_u(t) = m\ddot{z}(t), \tag{1}$$

where $f_e(t)$, $f_r(t)$, $f_b(t)$, $f_l(t)$, $f_s(t)$, and $f_u(t)$ are the excitation force, radiation force, buoyancy force, the losses force, the spring force, and the control force, respectively [15]. The constant m is the total mass of the PTO, which comprises the buoy, the rod, and the translator of the PMLG. The acceleration of the buoy is denoted as $\ddot{z}(t)$.

The excitation force, $f_e(t)$, is the major force that moves buoy, which is caused by the incident waves on the floating body. The excitation force is formulated using the following causal equation

$$f_e(t) = k_e(t) * \eta(t) = \int_{-\infty}^{t} k_e(\tau - t)\eta(\tau)d\tau, \tag{2}$$

where $\eta(t)$ and $k_e(t)$ are the wave elevation and excitation convolution kernel, respectively. The excitation convolution kernel in (2) can be linearly approximated using a transfer function $K_e(s)$ [16]. Therefore, Eq. (2) is written as

$$F_e(s) = K_e(s)H(s), \tag{3}$$

where $F_e(s)$ and $H(s)$ are the Laplace transforms of $f_e(t)$ and $\eta(t)$, respectively. The transfer function $K_e(s)$ is obtained using the following procedure. Numerical data are generated based on the parameters of the buoy and the sea. In this study, a hydrodynamic software system called WAMIT was used to generate the data [17]. The transfer function is formed by fitting the data using an identification method in the frequency domain.

The radiation force, $f_r(t)$, is the force applied by surrounding waves onto the submerged portion of the buoy. As proposed by [16], the time domain radiation force can be modelled as

$$f_r(t) = m_\infty \ddot{z}(t) + \int_0^t k_r(t - \tau)\dot{z}(t)d\tau, \tag{4}$$

where m_∞ and k_r represent the body added mass at the infinite frequency and the radiation convolution kernel, respectively. Similar to the excitation force, the convolution term in (4) can be approximated by a transfer function using the same procedure. In this study, the convolution term is modelled by a fourth order transfer function. Using this transfer function, the convolution term can be written in the state-space model as

$$\int_0^t k_r(\tau)\eta(t-\tau)d\tau \approx \mathbf{C_r}\mathbf{q_r}(t)$$
$$\dot{\mathbf{q}}_\mathbf{r}(t) = \mathbf{A_r}\mathbf{q_r}(t) + \mathbf{B_r}\dot{z}(t),$$

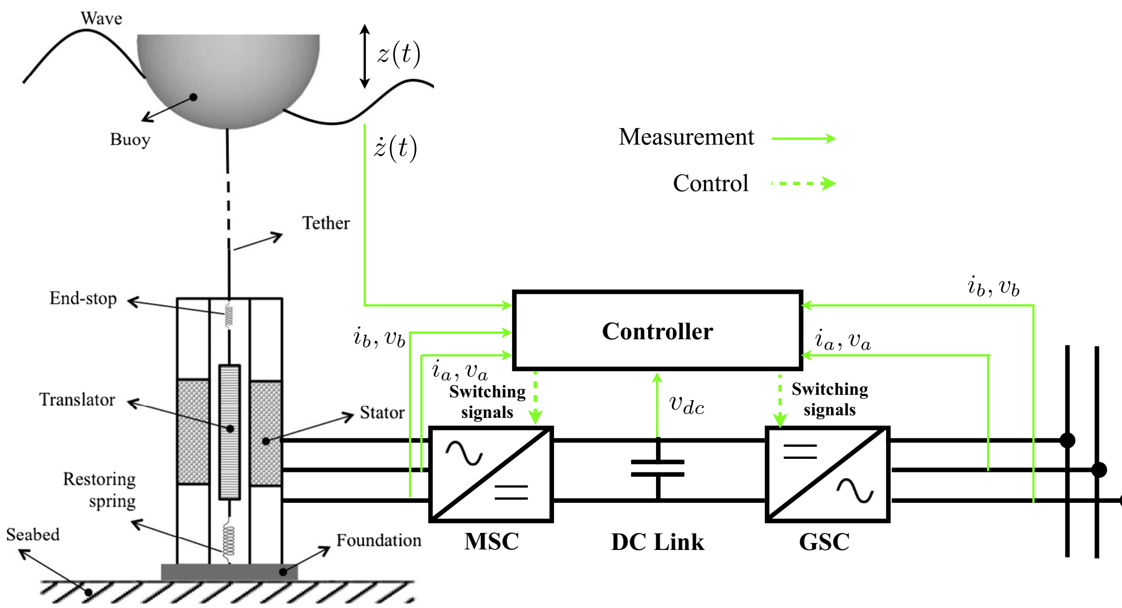

Fig. 1. Structure of the heaving WEC.

where $\dot{\mathbf{q}}_{\mathbf{r}}(t)$ is the fictitious radiation state vector, while $\mathbf{A_r}(t)$, $\mathbf{B_r}(t)$, and $\mathbf{C_r}(t)$ are the state, input, and output of the radiation force matrix, respectively. $f_r(t)$ is written in its state-space representation to facilitate its combination with the other forces that act on the buoy.

The buoyancy force, $f_b(t)$, is generated due to the motion of the floating body. For a freely oscillating body, $f_b(t)$ is proportional to the body displacement from the equilibrium point, which is

$$f_b(t) = S_b z(t), \tag{5}$$

where $S_b = \rho g A_w$ is the buoyancy stiffness coefficient. The constants ρ, g, and A_w are the sea water density, gravitational acceleration, and water plane area, respectively. The water plane area is formulated as

$$A_w = \begin{cases} \pi r^2, & \text{for cylindrical body} \\ \pi r^2\left(1 - \frac{|z(t)|^2}{3r^2}\right), & \text{for spherical body}, \end{cases}$$

where r is the radius of the oscillating body. For the conservative buoy's movements, the effect of the nonlinear term in A_w may be negligible for the spherical body. Therefore, A_w can be approximated as $A_w \approx \pi r^2$.

The spring force, $f_s(t)$, is the force obtained from the unit spring placed between the linearly moving translator and the seabed. Similar to $f_b(t)$, the spring force is modelled as a function of the buoy displacement

$$f_s(t) = S_s z(t), \tag{6}$$

where S_s is the spring coefficient.

The losses force, $f_l(t)$, combines all of the unknown and/or poorly known forces that can reduce the amount of power captured. For simplicity, this is modelled as a linear function

$$f_l(t) = R_{loss}\dot{z}(t), \tag{7}$$

where R_{loss} is the losses resistance.

Using the previous derivation, Eqs. (1)–(7) can be combined in the following state-space equation

$$\begin{aligned} \dot{\mathbf{x}}(t) &= \mathbf{A}\mathbf{x}(t) + \mathbf{B}(f_u(t) + f_e(t)) \\ \dot{z}(t) &= \mathbf{C}\mathbf{x}(t), \end{aligned} \tag{8}$$

where $\mathbf{x}(t) = [z(t)\ \dot{z}(t)\ \mathbf{q_r}(t)^T]^T \in \mathbb{R}^{6\times1}$ is the overall system state vector, and the state-space matrices, $\mathbf{A} \in \mathbb{R}^{6\times6}$, $\mathbf{B} \in \mathbb{R}^{6\times1}$, $\mathbf{C} \in \mathbb{R}^{1\times6}$ are

$$\mathbf{A} = \begin{bmatrix} 0 & 1 & \mathbf{0}_{1\times4} \\ \frac{-(\rho g A_w + S_s)}{m+m_\infty} & \frac{-R_l}{m+m_\infty} & \frac{-\mathbf{C_r}}{m+m_\infty} \\ \mathbf{0}_{4\times1} & \mathbf{B_r} & \mathbf{A_r} \end{bmatrix},$$

$$\mathbf{B} = \begin{bmatrix} 0 & 0 \\ \frac{1}{m+m_\infty} & \frac{1}{m+m_\infty} \\ \mathbf{0}_{4\times1} & \mathbf{0}_{4\times1} \end{bmatrix}, \quad \mathbf{C} = [0 \quad 1 \quad \mathbf{0}_{1\times4}].$$

2.2. Electrical model

The electrical model comprises the PMLG and the power converter module. Fig. 2 shows the d-q equivalent circuits of the PMLG, which represent the synchronous frame direct and quadrate components. The Park transformation is used to transform the three phase voltages and current quantities into the synchronous frame components [18]. The d-q components of the stator voltage, $v_s(t)$, at the terminal are formulated by the following equations

$$v_{sd}(t) = R_s i_{sd}(t) - \omega_e(t)\lambda_{sq}(t) + \frac{d}{dt}(L_{sd}i_{sd}(t) + \lambda_{PM}),$$

$$v_{sq}(t) = R_s i_{sq}(t) - \omega_e(t)\lambda_{sd} + \frac{d}{dt}(L_{sq}i_{sq}(t)),$$

$$\lambda_{sd}(t) = L_{sd}i_{sd}(t) + \lambda_{PM},$$

$$\lambda_{sq}(t) = L_{sq}i_{sq}(t),$$

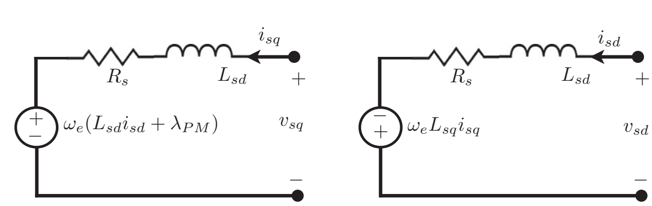

Fig. 2. Equivalent circuit of the PMLG.

where $i_s(t)$, R_s, and L_s are the stator current, the machine synchronous resistance and inductor, respectively. In this study, a surface-mounted PMLG is used. In this topology, the stator inductance quantities in the d-axis and the q-axis are almost identical, or $L_{sd} \approx L_{sq}$ [19]. The variables λ_{PM} and λ_s are the permanent magnet flux and the stator flux linkage, respectively. The variable $\omega_e(t)$ is the electrical angular frequency, which is given by the following equation

$$\omega_e(t) = \frac{2\pi \dot{z}(t)}{p_\omega},$$

where p_ω is the pole width of the PMLG. The converted (electrical) power, P_e, is given by

$$P_e(t) = \frac{3}{2} p \lambda_{PM} \omega_e(t) i_{sq}(t), \tag{9}$$

where p is the number of magnetic pole pairs. The stator active power, $P_s(t)$, and reactive power, $Q_s(t)$, are formulated as

$$P_s(t) = \frac{3}{2}(v_{sd}(t)i_{sd}(t) + v_{sq}(t)i_{sq}(t))$$
$$Q_s(t) = \frac{3}{2}(v_{sq}(t)i_{sd}(t) - v_{sd}(t)i_{sq}(t)).$$

The control force is implemented by altering the stator current in the PMLG using the back-to-back converter in the MSC. The currents $i_{sd}(t)$ and $i_{sq}(t)$ are controlled by regulating $v_{sd}(t)$ and $v_{sq}(t)$, respectively [19]. In order to minimize the copper losses, i_{sd} is set to zero [18]. The value of $i_{sq}(t)$ required to implement the control force is derived using the following procedure. The captured (mechanical) power, P_m, is formulated as

$$P_m(t) = f_u(t)\dot{z}(t). \tag{10}$$

If it is assumed that $P_e(t) = P_m(t)$, then we obtain the following

$$f_u(t)\dot{z}(t) = \frac{3}{2} p \lambda_{PM} \omega_e(t) i_{sq}(t).$$

Therefore, the current $i_{sq}(t)$ is

$$i_{sq}(t) = \frac{2 f_u(t)\dot{z}(t)}{3p\lambda_{PM}\omega_e(t)}. \tag{11}$$

In practice, there are physical constraints on implementing the current in (11) due to the rating of the power converter components or the thermal limits on the PMLG [18]. To consider these limitations, constraints are imposed on the voltages and currents. The maximum level of the stator current is defined on the maximum root mean squared value of the stator voltage v_s^{max}. The stator voltage of the PMLG is controlled by the dc-link voltage v_{dc}. In this study, the space vector pulse-width modulation is employed. Using this method, the relationship between v_s^{max} and v_{dc} can be obtained as

$$v_s^{max} = \frac{v_{dc}}{\sqrt{3}}.$$

Then, the maximum currents of d-q axis stator is formulated as

$$(-\omega_e(t)L_s i_{sq}(t))^2 + \left(L_s \frac{di_{sq}(t)}{dt} + \omega_e(t)\lambda_{PM}\right)^2 \leqslant (v_s^{max})^2.$$

By expanding the square in the last equation and omitting the second order derivative, the following Riccati equation is obtained

$$\frac{di_{sq}(t)}{dt} + \frac{\omega_e(t)L_s}{2\lambda_{PM}} i_{sq}^2(t) = \frac{v_s^{max} - \omega_e^2(t)\lambda_{PM}^2}{2\omega_e(t)\lambda_{PM}L_s}.$$

After solving the last equation, the maximum allowable i_{sq} is given by

$$i_{sq}^{max}(t) = \lim_{t\to 0}(i_{sq}(t)) \leqslant \frac{1}{X_s}\sqrt{(v_s^{max})^2 - (\omega_e(t)\lambda_{PM})^2}.$$

3. Controller design

An HCS comprises a HLC and a LLC. The HLC gives the reference velocity of the buoy $\dot{z}_r$, which is followed by the LLC. In the conventional HLC, $\dot{z}_r$ is generated using the following equation [9]

$$\dot{z}_r(t) = \frac{\hat{f}_e(t)}{2R_r}\cos\theta, \tag{12}$$

where R_r and θ are the system's radiation resistance and the phase difference between $\hat{f}_e(t)$ and $\dot{z}(t)$, respectively. The variable $\hat{f}_e(t)$ is the estimated value of $f_e(t)$, which is obtained from the system identified in the frequency domain, as described in Section 2.1. For simplicity, we assume that $\hat{f}_e(t)$ is equal to $f_e(t)$. If the LLC can track the reference, θ is equal to zero. In the conventional HCS, the constant R_r is obtained using hydrodynamic software, e.g., WAMIT, by employing the parameters of the buoy and the sea. The graph of R_r is generated over the operating frequencies. The designer chooses the value of R_r for use in (12) by selecting from the maximum value for R_r in all of the operating frequencies or in the most common peak frequency, ω_p, that may occur at the site.

For particular configuration of the WEC in Fig. 3, there are disadvantages when selecting a single value of R_r in (12) because this is only optimal at the selected ω_p. In more energetic sea states, the control force, $f_u(t)$, has a high level due to insufficient damping of $f_e(t)$, which is undesirable because we need to enlarge the size of the PTO, thereby increasing the investment costs to increase the maximum level of $f_u(t)$. In less energetic sea states, the power absorption is low because of the excessive damping of $f_e(t)$. In addition to the selection of R_r, the level of $f_u(t)$ is influenced by the dynamic or transfer functions for the model in the LLC. For example, a transfer function can be derived to link the error, $e(t)$, to the $f_u(t)$ in the LLC. Therefore, in order to design R_r to limit the maximum level of $f_u(t)$, it is not sufficient to design it in the HLC alone.

Thus, we propose the BU-HCS in order to avoid these issues. The control system configuration for the BU-HCS is depicted in Fig. 3. The objectives of the BU-HCS are as follows.

- Design the intrinsic resistance, R^*, to replace the R_r in (12), which can limit the maximum value of $f_u(t)$ in various wave peak frequencies and significant heights, regardless of the uncertainty in the system's model.
- The designed R^* considers the PTO utilization index, which is formulated as the ratio between the maximum value of the converted (electrical) power relative to the average converted power. A smaller ratio indicates efficient utilization (or appropriate sizing) of the PTO and a lower reactive content in the electrical power.
- Design a simple controller in the LLC to track the reference velocity and reduce the maximum level of the $f_u(t)$, despite the uncertainty in the model.

The control configuration of the BU-HCS is depicted in Fig. 3. In order to satisfy our objectives, the LLC is designed before the HLC. The detailed designs of the LLC and HLC are described in the following sections.

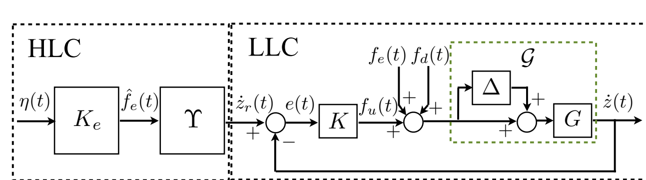

Fig. 3. Control system configuration of the proposed BU-HCS.

3.1. Lower level controller

The control configuration of the LLC is depicted in Fig. 3. The feedback control system in the LLC contains two transfer functions: $\mathcal{G}(s)$ and $K(s)$. $\mathcal{G}(s)$ and $K(s)$ are the transfer functions for the mechanical model of the WEC and the controller, respectively. In this study, $\mathcal{G}(s)$ comprises a nominal model of the plant $G(s)$ with an input multiplicative uncertainty. The transfer function $\Delta(s)$ represents the transfer function for uncertainties such as parameter perturbation and un-modelled dynamics or forces. The signal $f_d(t)$ represents an unknown external disturbance, which may alter the buoy's velocity.

The following procedure obtains a simple robust controller, which minimizes $f_u(t)$ and tracks the reference. For simplicity, the controller K is formulated as a simple structure lead-lag compensator, i.e.,

$$K(s) = k\frac{(s+z)}{(s+p)},$$

where the constants k, z, and p are the gain, zero, and pole, respectively. The parameters in the lead-lag compensator are designed according to the following small-gain theorem.

Theorem 1 [20]. *If $\Delta(s)$ is stable and $K(s)$ is the stabilizing controller for the closed-loop system, then the following holds*

$$\left\|\frac{\Delta(s)K(s)G(s)}{1+K(s)G(s)}\right\|_\infty < 1$$

or,

$$\left\|\frac{K(s)G(s)}{1+K(s)G(s)}\right\|_\infty < \frac{1}{\|\Delta\|_\infty} \quad \square$$

In order to stabilize the closed-loop system for the largest set of perturbation in $\Delta(s)$, the following minimization problem is obtained

$$\underset{K(s)\ \text{stabilizing}}{\text{minimize}} \left\|\frac{K(s)G(s)}{1+K(s)G(s)}\right\|_\infty. \tag{13}$$

The controller $K(s)$ obtained from the latter optimization ensures that robust stability is achieved.

The other performance specifications can be formulated within the framework of $\mathcal{H}_\infty$ theory using the nominal closed-loop system of the LLC in Fig. 3. The transfer function between the error and the velocity reference is formulated as

$$\frac{E(s)}{V_r(s)} = \frac{1}{1+G(s)K(s)},$$

where $E(s)$ and $V_r(s)$ are the Laplace transforms of $e(t)$ and $\dot{z}_r(t)$, respectively. This transfer function represents the tracking performance of the controlled system. It is obvious that minimizing ∞-norm for the latest transfer function while keeping $K(s)$ stable can provide a good indicator of the tracking performance of the controlled system, which can be formulated mathematically as

$$\underset{K(s)\ \text{stabilizing}}{\text{minimize}} \left\|\frac{1}{1+G(s)K(s)}\right\|_\infty. \tag{14}$$

The same idea can be applied to minimize the control force. The transfer function between the control force and the velocity reference is

$$\frac{F_u(s)}{V_r(s)} = \frac{K(s)}{1+G(s)K(s)},$$

where $F_u(s)$ is the Laplace transform of $f_u(t)$. Therefore, the following must be solved to achieve the minimal control force for the controlled system

$$\underset{K(s)\ \text{stabilizing}}{\text{minimize}} \left\|\frac{K(s)}{1+G(s)K(s)}\right\|_\infty. \tag{15}$$

By combining the problem statement for the robustness property in (13) and other performance considerations in (14) and (15), it is obvious that we need to solve all of the equations simultaneously to find the admissible lead-lag compensator parameters, as described by the following equation

$$\underset{K(s)\ \text{stabilizing}}{\text{minimize}} \left\|\begin{matrix}\frac{K(s)G(s)}{1+K(s)G(s)}\\ \frac{1}{1+G(s)K(s)}\\ \frac{K(s)}{1+G(s)K(s)}\end{matrix}\right\|_\infty. \tag{16}$$

The genetic algorithm optimization toolbox (GAOT) is used to find the parameters of the lead–lag compensator by solving the optimization problem in (16) [21,22]. GAOT provides flexibility to solve the optimization problem using various controller structures, which is an advantage compared with other $\mathcal{H}_\infty$ optimization solvers, e.g., the robust control toolbox in Matlab can only generate a full order controller. However, due to the heuristic property of GAOT, the solution produced might not be optimal. Thus, we could invest more effort to obtain another solver that provides the optimum solution of (16). The flowchart of the process required to find the parameters of the lead-lag compensator using GAOT is shown in Fig. 4.

3.2. Higher level controller

The HLC in Fig. 3 comprises two transfer functions. The transfer function $K_e(s)$ converts the wave elevation $\eta(t)$ into the estimated excitation force $\hat{f}_e(t)$, which can be found using the procedure in Section 2.1. It is assumed that the excitation force is equal to its estimated value, or $f_e(t) = \hat{f}_e(t)$. The reference velocity $\dot{z}_r(t)$ is generated using the transfer function $\Upsilon(s)$, which is simply formulated as

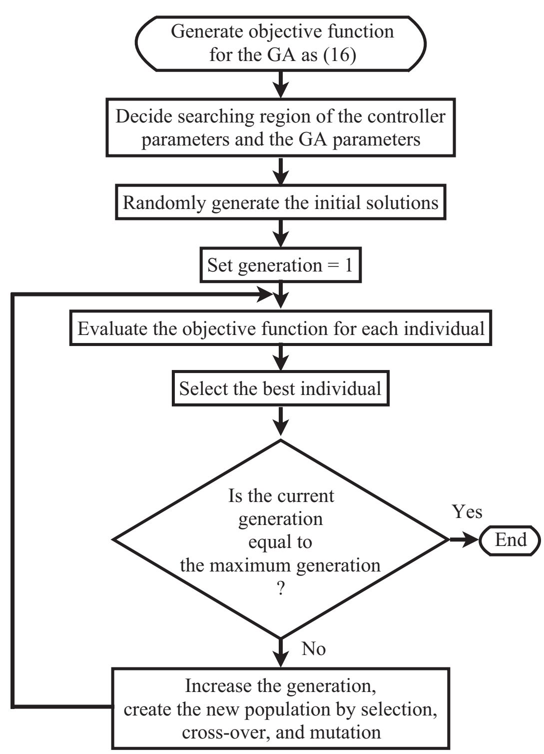

Fig. 4. Flowchart illustrating the process required to find the parameters of the lead-lag compensator using GAOT.

$$\Upsilon(s) = \frac{V_r(s)}{F_e(s)} = \frac{1}{R^*},$$

where $F_e(s)$ is the Laplace transform of $f_e(t)$ and R^* is the constant intrinsic resistance that need to be designed using the transfer functions in the HCS.

As mentioned earlier, the intrinsic resistance is designed so the maximum value of the control force f_{um} will not exceed its allowable value. This condition occurs in more energetic sea states, i.e., sea states with a higher significant height H_s and lower peak frequency ω_p. It is also desirable to design R^* to maintain the ratio between the average converted (electrical) power $\bar{P}_e$ and its maximum power P_{em} below a certain value. A higher ratio indicates a higher reactive power generated by the PTO, which represents the inefficiency of the PTO. A higher ratio of $P_{em}/\bar{P}_e$ tends to occur in less energetic sea states, where the sea states have a lower H_s and a higher ω_p.

The intrinsic resistance that satisfies the constraints can be designed using the transfer functions of $K_e(s)$ and $\Upsilon(s)$. The following equation can be derived using these transfer functions

$$\begin{aligned} F_u(s) &= \frac{K(s)}{1+G(s)K(s)} V_r(s) = \frac{K(s)}{1+P(s)K(s)} \frac{F_e(s)}{R^*(\omega)} \\ &= \frac{K(s)}{1+G(s)K(s)} \frac{F_e(s)H(s)}{R^*(\omega)}, \end{aligned}$$

where $H(s)$ is the Laplace transform of $\eta(t)$. By setting the control force to its maximum allowable value, $F_u(s)$ is equal to f_{um}. Hence, R^* can be obtained using the following equation

$$R^*(\omega) = \frac{K(s)}{1+G(s)K(s)} \frac{F_e(s)H(s)}{f_{um}}. \quad (17)$$

Note that the value of R^* in (17) changes with the frequency. In regular (monochromatic) sea states, $\eta(t)$ is sinusoidal wave form with specific H_s and ω_p. Therefore, R^* can be found using the Bode magnitude plot of the following transfer function,

$$R^*(\omega) = \left| \frac{K(s)F_e(s)}{1+G(s)K(s)} \frac{\eta_p}{f_{um}} \right| \quad (18)$$

where the constant η_p is equal to half of H_s, e.g., $\eta_p = 1$ for $H_s = 2$ m. Using the latter equation, a look-up table can be constructed for sea states with various heights and frequencies.

The intrinsic resistance in (18) will not violate the design value of f_{um} in the nominal system. However, any perturbation in the model tends to increase the value of $f_u(t)$ required in the LLC to maintain its tracking capacity. The more that the system deviates from its nominal value, the greater $f_u(t)$ becomes. The following procedure is conducted to maintain the maximum value of the control force below f_{um} in all scenarios and to satisfy the constraint on the ratio $P_{em}/\bar{P}_e$.

1. Find the value of R^* for specific values of f_{um} and H_s using (18) within the range of operation, ω_p.
2. Select the highest and the lowest values of R^*, and use these constants in the simulation, as depicted in Fig. 3 for the worst case scenario using a monochromatic sea state with specific values of H_s and ω_p.
3. Check the constraints on f_{um} and the ratio of $P_{em}/\bar{P}_e$ for both values of R^*.
4. If one of the constraints is violated, reduce the value f_{um} and go to (1); otherwise, stop the procedure.

This algorithm is a fast procedure for finding the value of R^* that satisfies the designed constraints. A look-up table can be generated using the Bode magnitude plot. This table gives the value of R^* based on the information for H_s and ω_p. In irregular (polychromatic) sea-states, this information can be obtained by performing the fast Fourier transform over the future sea states. This involves a prediction method, which is beyond the scope of this study. There is no need to change the value of R^* in a rapid sampling instant because the sea states will not change its profiles (i.e., H_s and ω_p) for a duration of 20–30 min [23].

3.3. Other methods for comparison

To facilitate comparisons, the WEC system was tested using various control techniques, i.e., conventional hierarchical control (C-HCS), reactive control (RC), resistive loading (RL), and the simplified bottom-up HCS (SBU-HCS). In C-HCS, the HLC is designed using (12) and the LLC employs the proposed lead-lag compensator. The value of R_r is selected from the maximum value over the operating frequency range. This method was used to compare the effect of HLC in providing the reference for the BU-HCS and C-HCS. The control force for the RC is formulated as

$$f_u(t) = -Z_{in}^*(\omega)\dot{z}(t),$$

where $Z_{in}(\omega) = R_{in}(\omega) + X_{in}(\omega)$ and $X_{in}(\omega) = \omega^2(m + M_r(\omega)) - (S_b + S_{rs})$. This RC is tuned at a single frequency of the wave. There are many other versions of RC methods that could be applied in this example, for example [24]. The control force for the RL differs slightly from the RC, as written in the following equation

$$f_u(t) = -|Z_{in}(\omega)|\dot{z}(t),$$

where

$$-|Z_{in}(\omega)| = \sqrt{(R_{in}(\omega))^2 + (X_{in}(\omega))^2}.$$

The RL is well-known for its high conversion rate between the captured (mechanical) power P_m and the converted (electrical) power P_e. The SBU-HCS is a simplified version of the BU-HCS, where the value of R^* is fixed for all sea state conditions, which further reduces the computational cost in the proposed BU-HCS. In this study, the SBU-HCS uses R^* in the highest value entry of the look-up table produced by the BU-HCS.

4. Simulation setup and results

4.1. Simulation setup

The parameters of the mechanical and electrical models are listed in Table 1. In this study, we used a spherical buoy. Using

Table 1
Parameters of the mechanical and electrical models.

Parameter (symbol)	Value [unit]
Buoy radius (r)	5 [m]
Buoy and translator mass (m_b)	2.68×10^5 [kg]
Infinite added mass (m_∞)	1.34×10^5 [kg]
Water plane area (A_w)	78.54 [m^2]
Submerged volume (V_s)	261.80 [m^3]
Sea water density (ρ)	1025 [kg/m^3]
Gravitational acceleration (g)	9.81 [m/s^2]
Seabed depth (d)	80 [m]
Resonance angular frequency (ω_0)	1.56 [rad/s]
Buoyancy stiffness coefficient (S_b)	7.89×10^5 [N/m]
Nominal restoring stiffness coefficient (S_{s0})	2×10^5 [N/m]
Initial losses resistance (R_{loss0})	0.4×10^5 [N s/m]
PMLG synchronous resistance (R_s)	0.29 [Ohm]
Permanent magnet flux (λ_{PM})	23 [Wb]
PMLG pole width (p_w)	0.05 [m]
DC link voltage (V_{dc})	3500 [V]
Modulation index (ma)	1

the design parameters in Table 1, the mechanical model in (9) was obtained, where the components of the radiation force were derived as the following matrices

$$\mathbf{A}_r = \begin{bmatrix} -3.4376 & -6.3533 & -4.9714 & -1.7168 \\ 1 & 0 & 0 & 0 \\ 0 & 1 & 0 & 0 \\ 0 & 0 & 1 & 0 \end{bmatrix}$$

$$\mathbf{B}_r = [1\ 0\ 0\ 0]^T$$

$$\mathbf{C}_r = [0.96 \times 10^5\ 3.62 \times 10^5\ 1.57 \times 10^5\ 0].$$

The following eighth order transfer function was used to model the transfer function of the excitation force $K_e(s)$, as described in Section 2.1

$$K_e(s) = \frac{(4.3\times10^5)s^8+(4\times10^5)s^7+\ldots}{s^8+0.8s^7+2.4s^6+\ldots}\ \frac{(1.1\times10^6)s^6+7.3\times10^5)s^5+\ldots}{1.3s^5+1.8s^4+\ldots}\ \frac{(8.8\times10^5)s^4+(3.6\times10^5)s^3\ldots}{0.5s^3+0.4s^2+\ldots}\ \frac{(2.1\times10^5)s^2+(4\times10^4)s-(6.1\times10^{-9})}{0.04s+0.01}. \quad (19)$$

Using the mechanical model obtained and the procedure in Section 3.1, the transfer function of the lead-lag compensator was formulated as the following equation

$$K(s) = 3 \times 10^6 \left(\frac{s+180}{s+2}\right). \quad (20)$$

In this simulation, we considered the sea states with $H_s = 1$–3 m and $\omega_p = 0.5$–1 rad/s. We assumed that the maximum level of the control force that could be generated by the PTO f_{um} was 1.5 MN. The ratio of $P_{em}/\bar{P}_e$ was designed to be less than 10. In the process used to obtain R^*, the designed value of f_{um} was reduced to 0.49 MN, 1 MN, and 1 MN for $H_s = 1$ m, 2 m, and 3 m, respectively, as explained in Section 3.2. The worst case scenario was used for designing R^* in BU-HCS. We assumed that in the worst scenario, the following occurred simultaneously.

- There are perturbation parameters in the restoring spring stiffness coefficient, S_s, and there is un-modelled losses resistance, R_{loss}. The perturbation in S_s is formulated as

$$S_s = S_{s0} + \Delta_s, \quad (21)$$

where S_{s0} and Δ_s are the nominal value of S_s and the percentage deviation of S_s from its nominal value, respectively. The perturbation in R_{loss} is formulated as

$$R_{loss} = R_{loss0} + \Delta_l, \quad (22)$$

where R_{loss0} and Δ_l are the initial value of R_{loss} and the percentage deviation of R_{loss} from its initial value, respectively. Note that R_{loss0} is called the initial value and not the nominal value because the nominal value of R_{loss} is equal to zero. In the worst case condition, Δ_s and Δ_l are set to 50% in (21) and (22).
- There is an un-modelled disturbance force, $f_d(t)$, which is formulated as

$$f_d(t) = -R_{loss0}\dot{z}(t) - S_{s0}z(t) - \alpha_d z(t)|z(t)|\sin(\omega_d t), \quad (23)$$

where $\alpha_d = 0.5 \times 10^4$ and $\omega_d = 0.5$ rad/s. Fig. 5 shows the plot of $f_d(t)$ in the irregular sea state, which can be considered as an aggressive disturbance because it has the same order as $f_e(t)$.

Using (19) and (20) and the procedure described in Section 3.2, Fig. 6 shows the magnitude of R^* for the specified values of H_s and ω_p. Table 2 shows an example of the look-up table obtained from Fig. 6. The value of R_r in the C-HCS was equal to 9×10^4 N s/m. The value of R^* for the SBU-HCS was selected from the highest values in Table 2, i.e., $R^* = 1.73 \times 10^6$ MNs/m for $H_s = 3$ m and $\omega_p = 0.5$ rad/s. This ensured that the design constraints were not violated when we used the selected R^* in the SBU-HCS. The RC and RL methods were tuned using a single frequency of incoming wave at $\omega_p = 0.75$ rad/s.

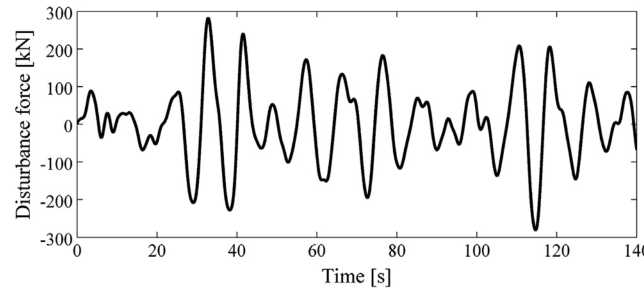

Fig. 5. Disturbance force in an irregular sea state with $H_s = 2$ m and $\omega_p = 0.75$ rad/s.

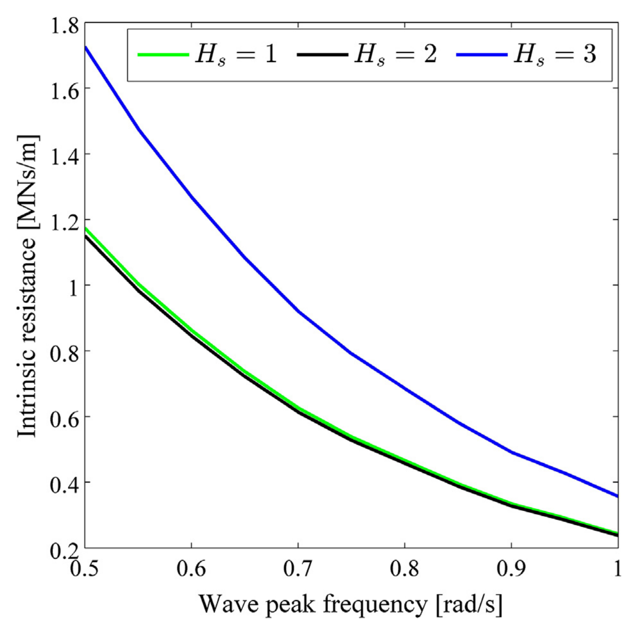

Fig. 6. Bode magnitude plot of R^* for various significant wave heights.

Table 2
Look-up table for the value of R^*.

ω_p [rad/s]	$H_s = 1$ [m]	$H_s = 2$ [m]	$H_s = 3$ [m]
0.50	1.17×10^6	1.15×10^6	1.73×10^6
0.55	1.00×10^6	9.84×10^5	1.48×10^6
0.60	8.63×10^5	8.46×10^5	1.27×10^6
0.65	7.34×10^5	7.22×10^5	1.08×10^6
0.70	6.27×10^5	6.14×10^5	9.21×10^5
0.75	5.38×10^5	5.28×10^5	7.91×10^5
0.80	4.66×10^5	4.58×10^5	6.86×10^5
0.85	3.96×10^5	3.88×10^5	5.82×10^5
0.90	3.34×10^5	3.28×10^5	4.92×10^5
0.95	2.97×10^5	2.85×10^5	4.27×10^5
1.00	2.43×10^5	2.38×10^5	3.57×10^5

The proposed method was tested using regular and irregular sea states as well as in the nominal and various perturbation cases. The irregular sea states were generated using the JONSWAP spectrum, and they were characterized by specific values of H_s and ω_p [25]. The values of ω_p used in this study ranged from $\omega_p = 0.5$ rad/s to $\omega_p = 1$ rad/s. The simulation was implemented using Matlab/Simulink with a sampling time of 1 ms.

4.2. Simulation results

The contents of this section are described as follows. First, we present the simulation results obtained using the regular (monochromatic) sea states under various control strategies in the nominal case. Thus, we demonstrate the effectiveness of the BU-HCS for selecting its R^* to improve the performance without violating the constraints compared with other control strategies. The test of regular sea states allows us to demonstrate the performance of the control strategies with specific values of H_s and ω_p. Next, we tested the BU-HCS alone using an irregular (polychromatic) sea state to demonstrate the tracking capacity of the BU-HCS. Finally, we tested the robust performances of the BU-HCS when subjected to parameter perturbations and in the presence of an un-modelled disturbance force. We compare the results obtained with those produced using other control strategies.

The simulation results obtained with a regular sea state for $H_s = 1$ m using the RC and C-HCS are shown in Fig. 7. Fig. 7a shows the average captured (mechanical) power, $\bar{P}_m$, in each of the waves, ω_p. The figure shows that for a fixed wave height, $H_s = 1$ m, large values of $\bar{P}_m$ could be obtained for all values of ω_p. However, the average converted (electrical) power, $\bar{P}_e$, in Fig. 7b shows that there was reverse power at low frequency waves. This condition is undesirable because the PTO receives the power rather than generating it. This also proves that the electrical model needs to analyze the performance of the WECs system because reversing can occur on the electrical (converted) power side. Fig. 7c shows the peak of the control force, f_{um}, in each ω_p. Both controllers reached the maximum limit of the force in the lower frequencies, which indicates that the R_r in the C-HCS was not sufficiently large to produce the damping force. The ratio of $P_{em}/\bar{P}_e$ in Fig. 7e was very high for both methods, which indicates the inefficiency of the PTO and the large reactive power content in the PTO. The percentage conversion efficiency between $\bar{P}_m$ and $\bar{P}_e$ is denoted as PTO's efficiency and shown in Fig. 7f. Both controllers exhibited poor performance in more energetic sea states due to the reversing power, whereas their performance improved in the less energetic sea states.

Thus, more severe conditions can be expected from the RC and C-HCS in more energetic sea states. The results obtained by both methods using the regular wave with $H_s = 3$ m are depicted in Fig. 8. In this scenario, reversing power occurred in both the captured and converted powers, as shown in Fig. 8a and b, respectively. Similar to the previous results, reversing power was exhibited by both methods in more energetic (lower peak frequencies) sea states. The maximum value of the control force reached its limit at all of the operating frequencies, as shown in Fig. 8c. In Fig. 8e, the ratio of $P_{em}/\bar{P}_e$ is higher compared with the result for the wave with $H_s = 1$ m. The conversion efficiency in Fig. 8f has the same trend as that shown in Fig. 7f.

The computer simulation results obtained for $H_s = 1$ m using the BU-HCS, SBU-HCS, and RL methods are shown in Fig. 9. There was no reversing in the average power with all methods, as

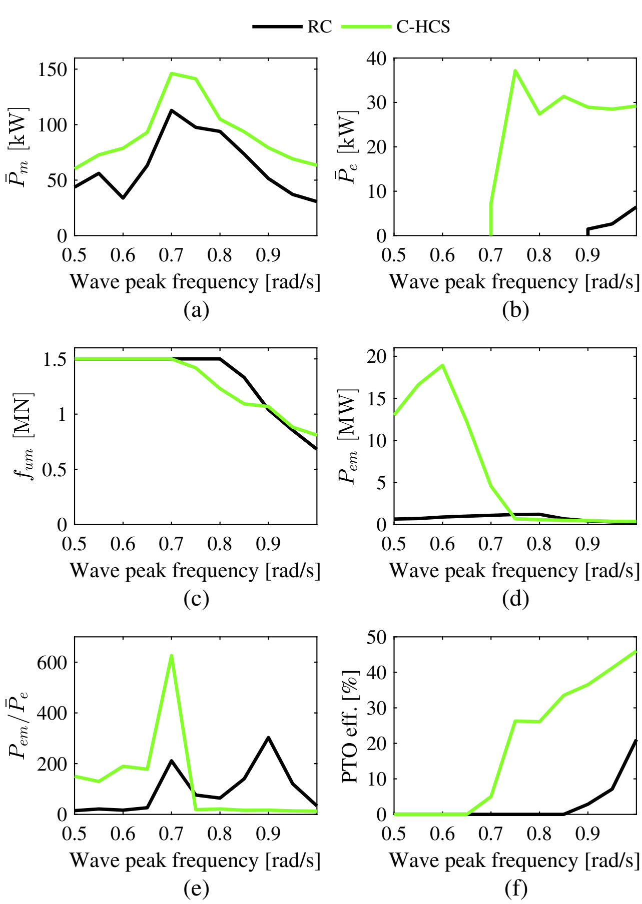

Fig. 7. Simulation results obtained using the RC and C-HCS for a regular sea state with $H_s = 1$ m.

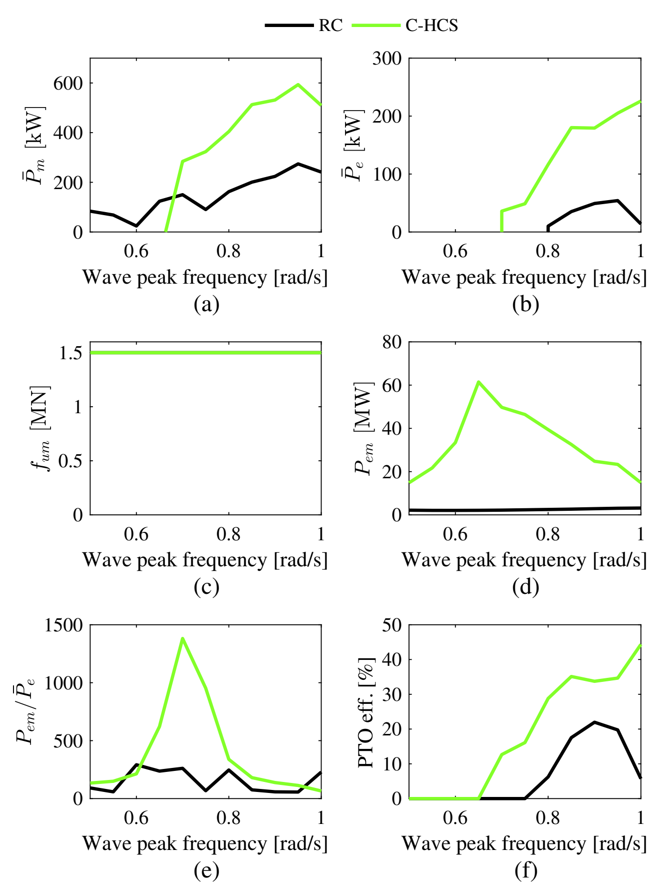

Fig. 8. Simulation results obtained using the RC and the C-HCS for regular sea states with $H_s = 3$ m.

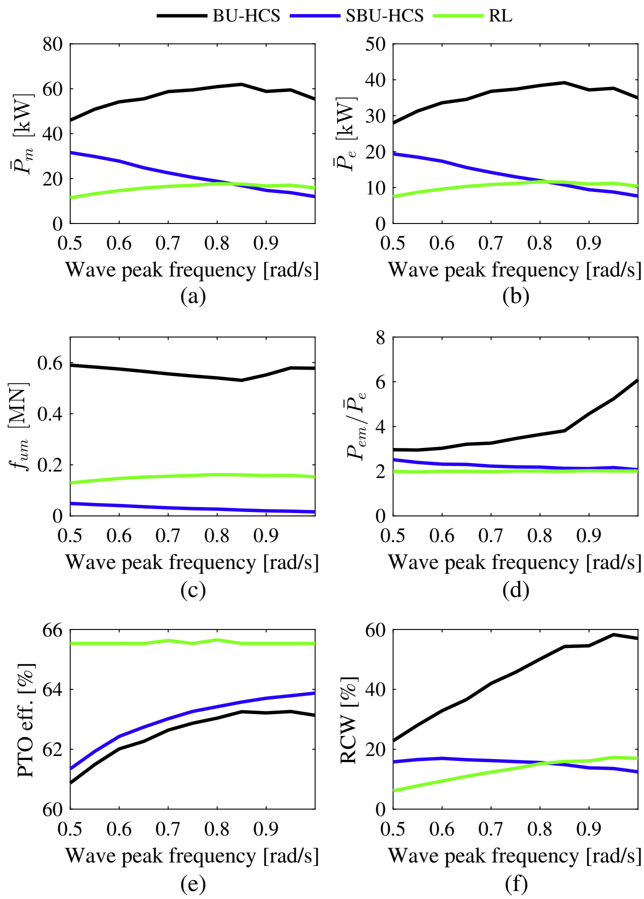

Fig. 9. Results obtained using the BU-HCS, SBU-HCS, and RL methods for regular sea states with $H_s = 1$ m.

depicted in Fig. 9a and b. The BU-HCS exhibited superior performance compared with the SBU-HCS and RL in terms of the captured and converted power when operating at all values of ω_p. The SBU-HCS outperformed the RL in more energetic sea states, but the opposite was true in less energetic sea states. This was because the fixed value of R^* was too high in the less energetic sea states. This was not the case for the BU-HCS, where the values of R^* could vary to adapt to changes in the sea states. Fig. 9c shows that the maximum level of the control force with all methods was far below the limit. For the BU-HCS, it was possible to reduce the value of R^* to increase $\bar{P}_m$ and thus $\bar{P}_e$. However, this would violate another constraint, i.e., the ratio of $P_{em}/\bar{P}_e$. The proposed R^* was sufficient to maintain the ratio below the designed value (i.e., 10), as depicted in Fig. 9d for the nominal and worst case scenarios. Therefore, the proposed values of R^* in the BU-HCS are the optimum values that satisfy the design constraints. The PTO's efficiencies for all of these methods are depicted in Fig. 9e. The RL method performed better than the BU-HCS and the SBU-HCS, but this superior conversion efficiency did not result in higher gains in $\bar{P}_m$ and $\bar{P}_e$, as shown in Fig. 9a and b. In order to see the performance of the proposed methods in term of converting the wave energy into the electrical power, we calculated the conversion using percentage of relative capture width (RCW). The RCW is formulated as

$$\mathrm{RCW} = \frac{\bar{P}_e}{P_w},$$

where P_w is the wave-power transport that is written as [9]

$$P_w = \frac{\rho g^2}{32\pi} T_p H_s^2 2r = (976\ \mathrm{W\ s^{-1}\ m^{-3}}) T_p H_s^2 2r.$$

The percentage of RCW for BU-HCS, SBU-HCS, and RL methods are shown in Fig. 9f. The performance of BU-HCS method increases as the ω_p is increased and outperformed the performances of SBU-HCS and RL methods. The SBU-HCS method had better performance compare to the RL method in the most operating ω_p except in the region of less energetic sea-states.

The computer simulation results obtained for more energetic regular sea states ($H_s = 3$ m) using the BU-HCS, SBU-HCS, and RL methods are shown in Fig. 10. In Fig. 10a and b, $\bar{P}_m$ and $\bar{P}_e$ are almost ten times higher compared with the results in Fig. 9a and b. The BU-HCS outperformed the SBU-HCS and RL in terms of $\bar{P}_m$ and $\bar{P}_e$ at all operating values of ω_p. For the BU-HCS, satisfactory results were achieved without violating the constraints, as shown in Fig. 10c and d. Unlike the case with $H_s = 1$ m, the constraint on the level of f_{um} dominated the algorithm to find R^* in the BU-HCS. In terms of the PTO's efficiency, Fig. 10e exhibits the same trend as Fig. 9e. The BU-HCS exhibited superior performance compare with the SBU-HCS in terms of the conversion efficiency because the values of R^* for the SBU-HCS in this case were higher than the values of R^* for the BU-HCS, except when $\omega_p = 0.5$ rad/s, where both methods had the same value of R^*. Fig. 10f showed the percentage of RCW. The similar trend was resulted as Fig. 9f.

Fig. 11 shows the velocity and displacement of the buoy using the BU-HCS method for the most energetic regular sea-state in our numerical example (i.e., $H_s = 3$ m and $\omega_p = 0.5$ rad/s). This result was intended to check whether the physical constraints were not violated. The figure shows the velocity reference was tracked well without causing extreme displacement of the buoy.

The simulation results obtained using an irregular sea state with the BU-HCS in the nominal case are shown in Figs. 12 and

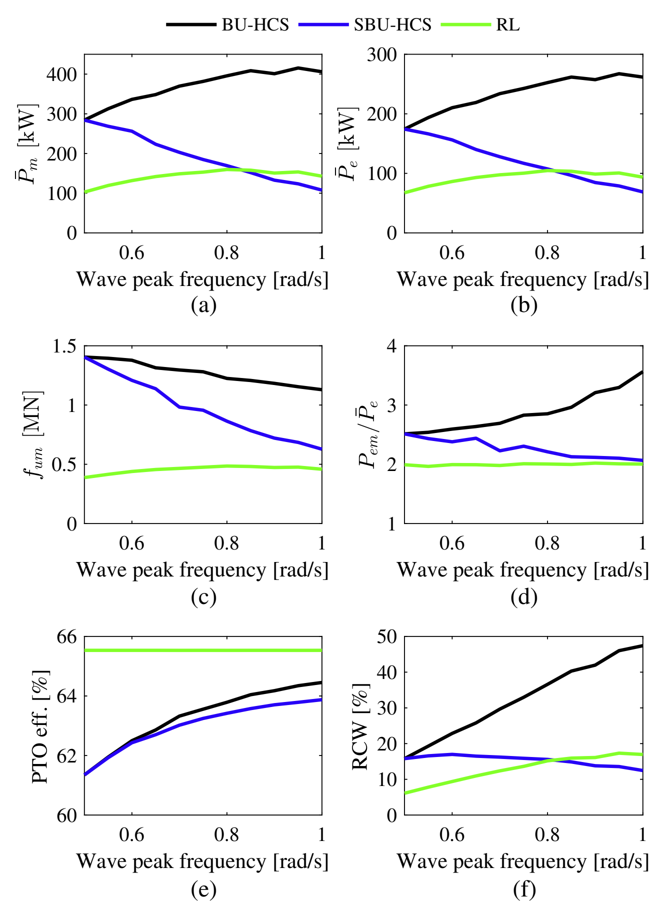

Fig. 10. Simulation results obtained using the BU-HCS, SBU-HCS, and RL methods for regular sea states with $H_s = 3$ m.

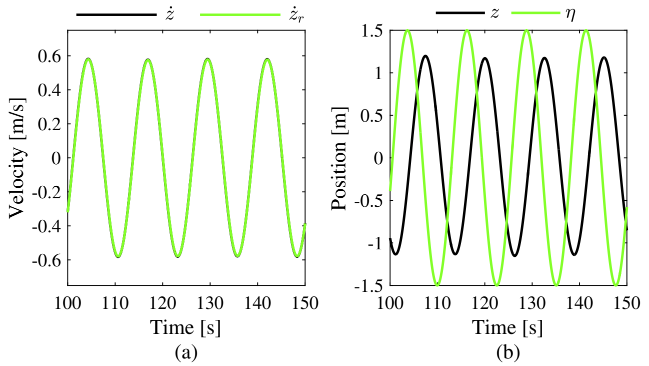

Fig. 11. Simulation results in terms of buoy's velocity and displacement obtained using the BU-HCS for the most energetic sea-state using regular sea state with $H_s = 3$ m and $\omega_p = 0.5$ rad/s.

13 for the mechanical and electrical quantities, respectively. The simulations used an irregular sea state with $H_s = 2$ m and $\omega_p = 0.75$ rad/s. The tracking capacity of the LLC is demonstrated in Fig. 12a, which shows that the velocity of the buoy, $\dot{z}(t)$, is almost equal to its reference, $\dot{z}_r(t)$. The value of the integral squared error (ISE) in the figure is equal to 3×10^{-4}, which indicates the almost perfect tracking capacity of the lead-lag compensator. Considering the radius of the buoy, the elevation of the buoy $z(t)$, and the wave elevation, $\eta(t)$, in Fig. 12b, we can conclude that there were no extreme movements of the buoy. Extreme movements must be avoided to prevent physical damage to the PTO. Fig. 12c compares $f_u(t)$ and $f_e(t)$. The control force had the same order of magnitude as $f_e(t)$ and it was below the design limitation. According to Fig. 12d, the average captured power, $\bar{P}_m$, generated 67.6 kW or 0.0676 MW. The d-q components of the stator voltage are shown in Fig. 13a. The q-axis current component, $i_{sq}(t)$, which was implemented with $f_u(t)$ in the linear generator, is shown in Fig. 13b. Fig. 13c shows the EMF voltage of the linear generator. The average converted power, $\bar{P}_e$, produced by the PTO was

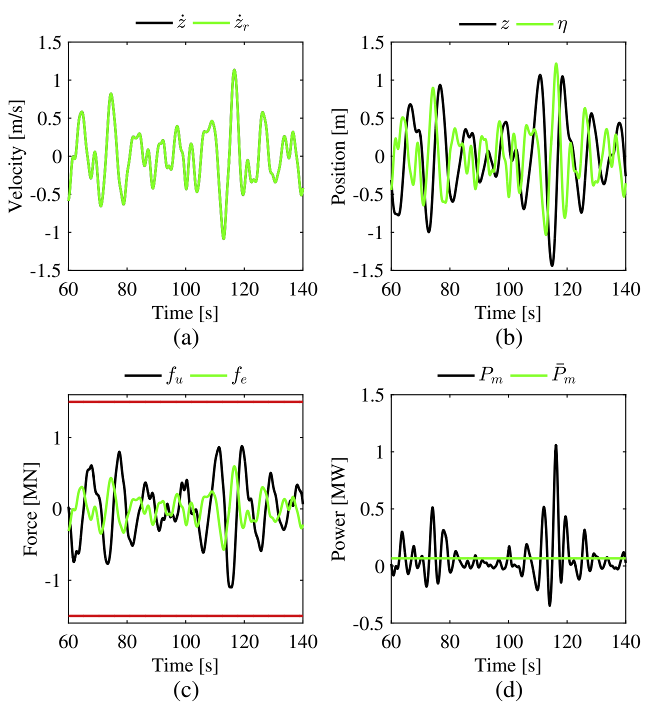

Fig. 12. Simulation results in terms of mechanical quantities obtained using the BU-HCS for an irregular sea state with $H_s = 2$ m and $\omega_p = 0.75$ rad/s.

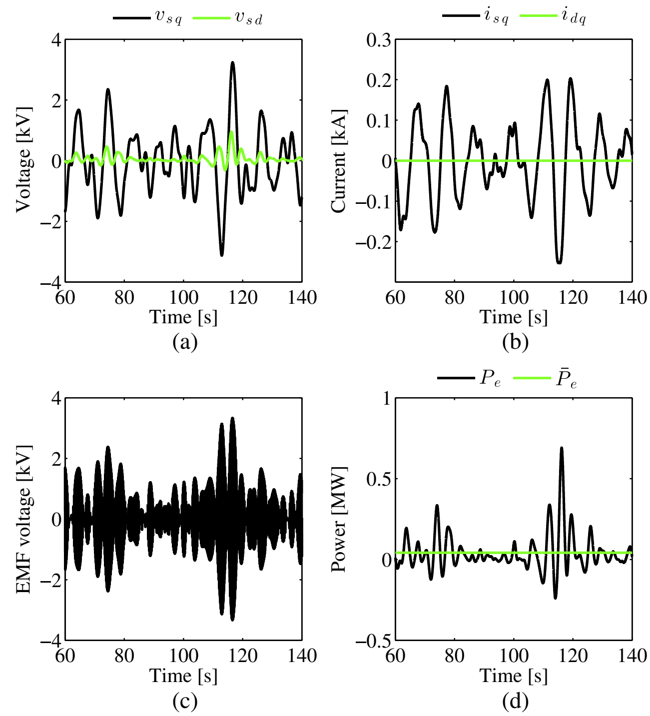

Fig. 13. Simulation results in electrical quantities obtained using the BU-HCS for an irregular sea state with $H_s = 2$ m and $\omega_p = 0.75$ rad/s.

42.3 kW or 0.0423 MW, as shown in Fig. 13d, which corresponds to a conversion efficiency of 62.6% between $\bar{P}_m$ and $\bar{P}_e$.

As mentioned in Section 4.1, the robustness property of the BU-HCS was tested against the parametric uncertainty in the spring force, f_s, and the un-modelled dynamics in the losses force, f_l. We assumed that the perturbations in f_s and f_l occurred simultaneously. Various perturbation scenarios were tested, as described in Table 3. In the nominal case, the value of $S_s = S_{s0}$ and the value of $R_{loss} = 0$. In case 1, the value of $S_s = S_{s0} + \Delta_s$ and $R_{loss} = R_{loss0} + \Delta_l$, where the value of $\Delta_s = \Delta_l = 0\,\%$. The values of Δ_s and Δ_l were varied up to 50%, as in case 9. The simulation was tested using an irregular sea state with $H_s = 2$ m and $\omega_p = 0.75$ rad/s for a duration of 140 s. In these different scenarios, the drop captured the energy measured in each case. To facilitate comparisons, the perturbation test was applied to the RL method.

The simulation results obtained for the WEC system using perturbations are summarized in Table 3. The BU-HCS captured more energy and experienced a lower electrical energy drop compared with the RL method. The drop in the energy was proportional to the increase in the perturbation of f_l. This is because the system with f_l had a higher damping force and thus the captured energy was lower compared with the nominal case. The ISE value between $\dot{z}(t)$ and $\dot{z}_r(t)$ in all perturbation scenarios was the same with the nominal case. This indicates robustness of the BU-HCS against the parameter perturbations.

Finally, we tested the WEC system against the worst case scenario, as described in Section 4.1. In this scenario, the system was tested in the presence of perturbation, as in case 9, as well as an un-modelled disturbance force, $f_d(t)$. In Fig. 5, the magnitude of $f_d(t)$ is one-third of the magnitude of $f_e(t)$. This test used the same irregular wave as the perturbation test in Table 3. The performance of the BU-HCS was again compared with that of the RL method. The BU-HCS obtained the same result as that for case 9 in Table 3, whereas the RL suffered a 32.2% loss in energy compared with the nominal case. This demonstrates that the BU-HCS is robust against the disturbance force.

Table 3
Various cases of perturbation scenarios in f_s and f_l.

Case	Δ_l [%]	Δ_s [%]	Energy [kWh]	Drop [%]
		BU-HCS		
Case 1	0	0	2.75	7.3
Case 2	0	25	2.75	7.3
Case 3	0	50	2.75	7.3
Case 4	25	0	2.45	10.9
Case 5	25	25	2.45	10.9
Case 6	25	50	2.45	10.9
Case 7	50	0	2.38	13.4
Case 8	50	25	2.38	13.4
Case 9	50	50	2.38	13.4
		RL		
Case 1	0	0	0.90	3.7
Case 2	0	25	0.85	5.6
Case 3	0	50	0.80	11.1
Case 4	25	0	0.84	6.7
Case 5	25	25	0.80	11.1
Case 6	25	50	0.75	16.7
Case 7	50	0	0.83	7.78
Case 8	50	25	0.78	13.3
Case 9	50	50	0.74	17.8

5. Conclusion

In this study, we proposed the novel BU-HCS method for heaving WECs. We described a simple and fast algorithm for generating the reference for the LLC. Our results showed that the proposed reference effectively improved the captured and converted power without violating the constraints on the maximum value of the control force and the PTO utilization index. A simple lead-lag compensator was designed to track the reference, which improved the robustness of the controlled systems and minimized the control force. The performance of the BU-HCS was better compared with existing methods in many nominal and perturbation scenarios. Hence, the proposed method provides an alternative solution to enhance the performance of heaving WECs.

The proposed BU-HCS has potential to be applied in a real application. This because the HLC is just a look-up table and the LLC is a fixed controller. Both of controllers are designed in off-line before the operation of the WECs. However, the BU-HCS requires an update information of incoming wave in term of its H_s and ω_p for every 20–30 min. This will require an additional computational resource to make online prediction method for the incoming wave. The online prediction method can be neglected by employing the SBU-HCS where all parameters were fixed. As the consequences on neglecting the online prediction method, the obtained electrical power is slightly higher compared to the power generated by the conventional RL method.

Acknowledgments

We thank the United Arab Emirates University (UAE-U) for supporting this research through the following grants: UAE-U Program for Advanced Research (No. 31N164) and UAE-U Start-up Grants (No. 31N159).

References

[1] International Energy Agency (IEA). Implementing agreement on ocean energy systems (IEA-OES). Annual report; 2012.
[2] Cruz J. Ocean wave energy, current status and future perspectives. Berlin, Germany: Springer; 2010.
[3] Alcorn R, O'Sullivan D. Electrical design for ocean wave and tidal energy systems. London, United Kingdom: The Institution of Engineering and Technology; 2013.
[4] Jaen A, Andrade D, Santana A. Increasing the efficiency of the passive loading strategy for wave energy conversion. J Renew Sustain Energy 2013;5:053132.
[5] Jama M, Wahyudie A, Assi A, Noura H. An intelligent fuzzy logic controller for maximum power capture of point absorbers. Energies 2014;7:4033–53.
[6] Schoen M, Hals J, Moan T. Wave prediction and robust control of heaving wave energy devices for irregular waves. IEEE Trans Sustain Energy 2011;26:627–38.
[7] Li G, Belmont M. Model predictive control of sea wave energy converters—part ii: the case of an array of devices. Renew Energy 2014;68:540–9.
[8] Richter M, Magana M, Sawodny O, Brekken T. Nonlinear model predictive control of a point absorber wave energy converter. IEEE Trans Sustain Energy 2013;4:118–26.
[9] Falnes J. Ocean waves and oscillating systems. Cambridge University Press; 2002.
[10] Jama M, Noura H, Wahyudie A, Assi A. Enhancing the performance of heaving wave energy converters using model-free control approach. Elsevier J Renew Energy 2015;83:931–41.
[11] Fusco F, Ringwood J. A simple and effective real-time controller for wave energy converters. IEEE Trans Sustain Energy 2014;4:21–30.
[12] Fusco F, Ringwood J. Hierarchical robust control of oscillating wave energy converters with uncertain dynamic. IEEE Trans Sustain Energy 2014;5:598–966.
[13] Brekken T. On model predictive control for a point absorber wave energy 174 converter. In: IEEE Trondheim PowerTech, Trondheim, Norway. p. 1–8.
[14] Wahyudie A, Jama M, Saeed O, Noura H, Assi A, Harib K. Robust and low computational cost controller for improving captured power in heaving wave energy converters. Elsevier J Renew Energy 2015;82:114–24.
[15] Falcao O. Wave energy utilization: a review of the technologies. Elsevier J Renew Sustain Energy Rev 2010;14:899–918.
[16] Taghipoura R, Pereza T, Moan T. Hybrid frequency-time domain for dynamic response analysis of marine structures. Elsevier J Ocean Eng 2008;4:685–705.
[17] WAMIT. User manual. Wamit Inc.
[18] Sul SK. Control of electric machine drive systems. Wiley; 2011.
[19] Feng W, Zhang X, Ju P, Sterling M. Modeling and control of AWS-based wave energy conversion system integrated into grid. IEEE Trans Power Syst 2008;23:196–204.
[20] Gu D, Petkov P, Konstantinov M. Robust control design with MATLAB. Springer; 2005.
[21] Houck C, Joines J, Kay M. A genetic algorithm for function optimization. NCSU-IE TR 95-09; 1995.
[22] Nandar CSA, Ngamroo I, Kunakorn A, Dechanupaprittha S, Watanabe M, Mitani Y, et al. Inverse additive perturbation-based optimization of robust PSS in an interconnected power system with wind farms. In: The proceeding of SICE annual conference. p. 237–40.
[23] Tucker M. Waves in ocean engineering: measurement, analysis, and interpretation. Ellis Horwood LTD; 1991.
[24] Korde U. Efficient primary energy conversion in irregular waves. Elsevier J Ocean Eng 1999;26:625–51.
[25] Kumar V, Kumar K. Spectral characteristic of high shallow water waves. Elsevier J Ocean Eng 2008;35:900–11.